Materials and Design 107 (2016) 18–25

Contents lists available at ScienceDirect

Materials and Design

journal homepage: www.elsevier.com/locate/matdes

Rational design of a material for rapid colorimetric Fe^{2+} detection

Nadia O. Laschuk [a], Iraklii I. Ebralidze [a], Simone Quaranta [a], Stephen T. W. Kerr [a], Jacquelyn G. Egan [a], Scott Gillis [a], Franco Gaspari [a], Alessandro Latini [b], Olena V. Zenkina [a,*]

[a] *Faculty of Science, University of Ontario Institute of Technology, 2000 Simcoe Street North, Oshawa, ON L1H 7K4, Canada*
[b] *Dipartimento di Chimica, Università degli Studi di Roma "La Sapienza", Piazzale A. Moro 5, Rome 00185, Italy*

ARTICLE INFO

Article history:
Received 4 April 2016
Received in revised form 1 June 2016
Accepted 6 June 2016
Available online 7 June 2016

Keywords:
TiO$_2$
Screen-printed films
Terpy
Iron detection

ABSTRACT

We report on the rational design of a novel TiO$_2$ based screen-printed material suitable for sensitive and selective detection of iron ions in water. This includes the synthesis and characterization of large mesoporous TiO$_2$ nanostructures, screen-printing of thick titania films on glass surfaces and their functionalization with 2,2′:6′,2″-terpyridin-4′-ylphosphonic acid (terpy). The ultra-high affinity between iron ions and the TiO$_2$-anchored terpy receptor makes this system potentially applicable to the analysis of iron in environmental, food, biological, and biomedical systems by a readily quantifiable colour change. Rapid (<30 s) colour change of the material from white to magenta permits easy detection of as low as 0.3 ppm of Fe^{2+} by the naked eye. The intensity of the colour change depends on the nature of the nanoparticles, the overall TiO$_2$ film thickness, and the Fe^{2+} concentration. The material was characterized using profilometry, diffuse reflectance UV–vis spectroscopy, and X-ray photoelectron spectroscopy (XPS) before and after treatment with aqueous solutions of Fe^{2+}. The designed material shows colour reversibility upon treatment with EDTA solutions, which allows for multiple reuses of the same film with no effect on sensitivity.

1. Introduction

Inexpensive and rapid detection and quantification of metal cations in aqueous solutions is in high demand for a variety of environmental, industrial, forensic, biological, and health applications. Especially interesting are systems that allow colorimetric detection to be performed by untrained personnel in field conditions by the naked eye [1,2]. Thus, the development of materials for this purpose is crucial [3]. Incorporation of sensing receptors on solid supports is a very promising strategy for the development of this type of materials. The most common approach is the integration of the functional motif of interest, for example a sensing receptor, into a polymeric matrix or formation of self-assembled monolayers (SAMs) containing a sensing receptor on the surface by utilization of an appropriate linker. Various derivatives of 2,2′:6′,2″-terpyridine (terpy) have been developed and implemented as such sensing receptors as summarized in seminal works by Constable [4] and Hancock [5]. Terpy based molecules were utilized to identify various metal cations [5–7] and cation-anion pairs [8,9]. To adjust polarity and therefore solubility, as well as to enhance sensing characteristics, terpy motifs have been combined into a variety of organic, organometallic, and supramolecular architectures. These structures were applied for metal ion sensing [10–12], counter anion sensing [8,13,14], sensing of bio-molecules [15,16], and for bio-imaging [17]. Incorporation of terpy derivatives into polymeric matrices often results in the formation of functional materials that can be employed as effective sensors [18]. For example, solutions of polyiminofluorene based polymer decorated with terpy groups were utilized as a highly sensitive and specific fluorimetric zinc sensor in organic solvent media [10]. Very recently, Garcia et al. reported the incorporation of the terpy motif into water soluble acrylic polymers for colorimetric detection of Fe^{3+}, Co^{3+}, Sn^{2+}, and Cu^{2+} in solution and on solid film [19]. In addition, they reported on the design of polymeric materials that are able to detect the sub-micromolar amounts of Fe^{3+} and Co^{3+} and micromolar amounts of Cu^{2+} and Sn^{2+}. Remarkably, varying the amount of terpy incorporated into the polymer allows for the effective tuning of the selectivity of the resulting polymeric material towards ion sensing. Moreover, a terpy-functionalized poly(ionic liquid) has been utilized for coordination and selective recognition of europium ions that can be further employed in the preparation of novel luminescent materials [20,21].

Besides the successful integration of terpy into soft materials and polymers, incorporation of this functional component into solid supports is an important step for the creation of materials for molecular electronics and photonics [22], electrochromic materials [23], and solar cells. Terpy motifs have been anchored onto a large number of solid supports resulting in functional materials with enhanced stability and excellent light absorption properties [18,23–29]. Nishihara et al. have achieved long range electron transport for molecular electric wires by assembling bis(terpyridine) metal complexes on gold surfaces.

---

* Corresponding author.
E-mail address: olena.zenkina@uoit.ca (O.V. Zenkina).

http://dx.doi.org/10.1016/j.matdes.2016.06.016
0264-1275/

Successively, they have used the same molecular motif to create electrochromic responsive nanostructures on the water-organic interface [30,31]. Terpy based macroligands were used to prepare yellow-green emitting Zn^{2+} metallo-polymer complexes with advanced photophysical properties for OLED applications [32]. Finally, the recent work of Li and Han shows that immobilization of nonplanar terpy motifs on graphene based porous materials through an azide-alkyne "click" reaction enhances porosity and carbon dioxide gas sorption capacity [33].

It is well documented that the terpy motif allows for visual differentiation between iron cations due to a rapid colour change from colourless to deep magenta, and this effect has been widely employed for the determination of Fe^{2+}. Remarkably, after more than 80 years since the discovery of the first Fe^{2+} terpy complex [34], the use of terpy derivatives for sensing of Fe^{2+} has mostly been performed in organic solvents or their mixtures with water [11,34–36]. To the best of our knowledge, a limited amount of truly water operational terpy based metal sensing systems have been reported [19]. In this paper we report the design of a novel material based on terpy-functionalized screen-printed TiO_2 films, able to detect Fe^{2+} in water.

2. Experimental

2.1. Materials

Titanium (IV) isopropoxide (TIP) (Vertec, 97 + %) and Ethylenediaminetetraacetic acid disodium salt dihydrate (99 + %), were purchased from Alfa Aesar. Ethanol (absolute, ≥99.8%), anhydrous terpineol, 5–15 mPa s ethyl cellulose (48.0–49.5% w/w ethoxyl basis), 30–70 mPa s ethyl cellulose (48.0–49.5% w/w ethoxyl basis), and titanium (IV) oxide (anatase nanopowder, <25 nm particle size) were purchased from Sigma Aldrich. Aeroxide VP P90 fumed titanium dioxide was kindly donated by Evonik. 2,2′:6′,2″-terpyridin-4′-ylphosphonic acid was synthesized according to previously published procedures [25,37–39].

2.2. Methods

2.2.1. The morphology of SAM anchored surfaces

STM images were recorded on Nanosurf NaioSTM using Nanosurf Naio 3.4.0 software. All STM images were obtained in the constant current mode by applying a tunneling current, I_t of 70 to 250 pA and a sample bias, V_t of 200 to 800 mV. The STM tips were mechanically cut from Pt/Ir wire (80/20, diameter 0.25 mm, Nanoscience). The calibration of the piezoelectric positioners was verified by atomic resolution imaging of graphite.

2.2.2. Surface coverage determination

UV–vis spectroscopy was used to determine the molecular density of monolayer films deposited on 1 mm quartz substrates as previously reported [40]. The instrument used for these experiments was a dual-beam Varian Cary® 50 UV–vis spectrophotometer, with a modified sample holder for thin film measurements. Assuming uniform distribution of Fe**L**$_2$ molecules on the surface and also that the extinction coefficient in solution and in a monolayer is the same, we can relate the absorbance spectra with a calculated surface concentration, rewriting the Beer–Lambert law as follows:

$$\Gamma_{\text{monolayer}}\left[\text{molecules}\cdot\text{cm}^{-2}\right] = \frac{A\cdot 10^{-3}\left[\text{cm}^{-3}\right]\cdot N_{Av}\left[\text{molecules}\cdot\text{mol}^{-1}\right]}{2\cdot\varepsilon\left[\text{M}^{-1}\text{cm}^{-1}\right]} \quad (1)$$

Here $\Gamma_{\text{monolayer}}$ is surface concentration, A is the monolayer absorbance, N_{Av} is Avogadro's number, and ε is the molar extinction coefficient. The factor of 2 in the denominator was implemented since the quarts slides were functionalized on both sides.

The peak at 560 nm, characteristic to Fe**L**$_2$, gives a molar extinction coefficient in solution of 11970 M^{-1} cm^{-1}. The monolayer absorbance for this Fe**L**$_2$ sample was 0.0029.

$$\Gamma_{\text{monolayer}} = \frac{0.0029\cdot 10^{-3}\left[\text{cm}^{-3}\right]\cdot 6.02\cdot 10^{23}\left[\text{molecules}\cdot\text{mol}^{-1}\right]}{2\cdot 11970\left[\text{M}^{-1}\text{cm}^{-1}\right]} = 7.29\cdot 10^{13}\left[\text{molecules}\cdot\text{cm}^{-2}\right]\approx 0.7\left[\text{molecules}\cdot\text{nm}^{-2}\right] \quad (2)$$

This corresponds to an area of $1/0.7 = 1.43$ nm^2 per molecule. That is close to 1.21 nm^2 per molecule determined from the crystal structure [41].

The peak at 313 nm was chosen to estimate surface coverage of the ligand. This peak of **L** gives a molar extinction coefficient in solution of 4910 M^{-1} cm^{-1}. The monolayer absorbance for this sample of **L** was 0.002. Analogously, surface concentration of the **L** is 1.23 [molecules·nm^{-2}] that corresponds to $1/1.23 = 0.81$ nm^2 per molecule.

2.2.3. Anchoring of **L** onto TiO_2 Nanoparticles (NPs): preparation of **L**-TiO_2 NPs

Immobilization of **L** was accomplished by stirring the suspension of TiO_2 anatase NPs (200 mg) with a solution of **L** (40 mg, 0.127 mmol) in DI water (40 mL). The mixture was stirred for 24 h at room temperature. After, the suspension was separated by centrifugation and the liquid part was removed. The solid residue was thoroughly washed with DI water (3 × 50 mL), centrifuged, decanted, washed with ethanol (3 × 50 mL), and dried in vacuum for 24 h.

2.2.4. Reaction of **L**-TiO_2 NPs with Fe^{2+} solution

Suspension of **L**-TiO_2 NPs was reacted with 40 mL of 45 ppm solution of Fe^{2+} in DI water. The mixture was stirred for 24 h at room temperature. **L**-TiO_2 NPs change colour from white to deep pink within 30 s. Further stirring in the solution of Fe^{2+} in DI water had no influence on the NPs colour. After, the mixture was separated by centrifugation. The deep magenta solid residue was thoroughly washed with DI water (6 × 50 mL), and ethanol (3 × 50 mL), centrifuged, and decanted. Solid precipitate was than dried in vacuum for 24 h.

2.2.5. Characterization of bare and **L**-TiO_2 anatase NPs

Bare and **L**-TiO_2 anatase NPs were characterized using Hitachi H7000 Transmission Electron Microscope operating under iTEM 5.2 software.

2.2.6. Syntheses and deposition of titanium dioxide scaffolds

Mesoporous titanium dioxide beads (mesoporous TiO_2 NPs) have been obtained by hydrothermal synthesis according to the procedure reported in Chen et al. [42] and Latini et al. [43]. Briefly, titanium tetraisopropoxide hydrolysis was conducted in a hydroethanolic medium using hexadecylamine and KCl as a templating agent and ionic strength buffer, respectively. Autoclaving and annealing conditions have been previously reported [43]. Screen-printing paste comprised of titanium dioxide mesoporous beads (scaffold material), ethyl cellulose (binder and thickener), and α-terpineol (solvent) has been prepared according to Ito et al. [44] and screen-printed on clean soda lime glass or FTO covered glass. Scaffold's film thickness was adjusted by one by one printing of several layers. Furthermore, commercially available high surface area P90 titanium dioxide was implemented into the paste as a scaffold material and screen-printed for comparison.

2.2.7. Mesoporous TiO_2 NPs characterization

Powder X-ray diffraction analysis of mesoporous TiO_2 beads has been carried out by using a Panalytical X'Pert PRO MPD diffractometer equipped with Cu Kα source (λ = 0.154184 nm) and a X'Celerator 1D RTMS silicon strip detector. The angular resolution (in 2θ) is 0.001°. Beam divergence, peaks asymmetry, and beam width have been adjusted by using a 0.04 rad soller slit, a 1° divergence slit, and a 20 mm mask on the incident beam path. Low background level and beam collimation have been assured by using a 6.6 mm anti-scatter slit and a 0.04 rad collimator on the diffracted beam path. Rietveld refinement analysis has been performed through MAUD software [45]. Scanning electron microscope images of the samples have been collected by using a Zeiss Auriga FE-SEM microscope. Specific surface area has been determined by using an ASAP 2020 Accelerated Surface Area and Porosimetry Analyzer (Micrometrics Instrument Corporation, U.S.) through the BET (Brunauer-Emmett-Teller) procedure. Pore size distribution has been determined by the BJH (Barret-Joyner-Halenda) method by the desorption branch of the isotherm.

2.2.8. Anchoring of **L** onto TiO_2 screen-printed films

Screen-printed films of TiO_2 on glass or ITO/glass were immersed into solution of **L** (20 mg, 0.064 mmol) in 100 mL of DI water. After 30 min films were copiously washed with DI water and isopropanol (4 × 4 mL) and dried by a stream of air or N_2. The same procedure was applied after each regeneration cycle.

2.2.9. Characterization of screen-printed films

Tencor Alpha-Step-200 profilometer was equipped with a standard stylus of 12.5 μm radius. Sample leveling was automatically computed after each scan and digitized using GetData Graph Digitizer 2.24 software. Typical scan lengths were 10,000 μm. Diffuse reflectance measurements have been performed on the bare, *N*-aromatic ligand sensitized and iron adsorbed films. The spectra have been collected in the range 280–1200 nm in transmittance mode using a double-beam Lambda 750S spectrophotometer (Perkin-Elmer, U.S.) equipped with a 60 mm integrating sphere. XPS measurements were performed using a Thermo Scientific K-Alpha surface analysis system equipped with a monochromated Al Kα X-ray source (1486.7 eV). Ultrahigh vacuum (UHV) conditions (10^{-9} to 10^{-10} Torr) were maintained during the experiment. The instrument is fitted with a flood source for an effective charge compensation. The Ti^{4+} $2p_{3/2}$ peak of TiO_2 at 458.6 eV was used as an internal reference peak for calibrating the binding energy. A Smart fit algorithm was used for background subtraction and a Powell peak-fitting algorithm for data analysis. The elemental ratio was determined using Wagner atomic sensitivity factors [46].

3. Results and discussion

Recently, we utilized 2,2′:6′,2″-terpyridin-4′-ylphosphonic acid (**L**), which is able to interact with a number of metal ions via its *N*-aromatic terpy moiety, for the selective detection of Fe^{2+}, Fe^{3+}, Ru^{3+}, and Zn^{2+} in aqueous media [41]. Reliable and fast quantification of 50 ppb to 1 ppm levels of each target cation was demonstrated in solution. In this paper we report the embedding of terpy based water soluble receptors onto hydrophilic quartz, fluorine-doped tin oxide (FTO) coated glass, TiO_2 nanoparticles, and screen-printed porous surfaces, and explore the performance of these novel materials as Fe^{2+} sensors. The phosphonate functional group not only makes **L** water soluble, but allows for the formation of robust self-assembled monolayers on a variety of surfaces. Thus, phosphonates have been utilized for the surface modification of a wide range of oxide substrates [47] such as titania [48,49], alumina [50], iron oxides [51], hafnium oxide [52], indium-tin oxide (ITO) [53], and silica [54]. Phosphonate-anchored SAMs are easily prepared in air, and form well-ordered strongly bound films on oxide

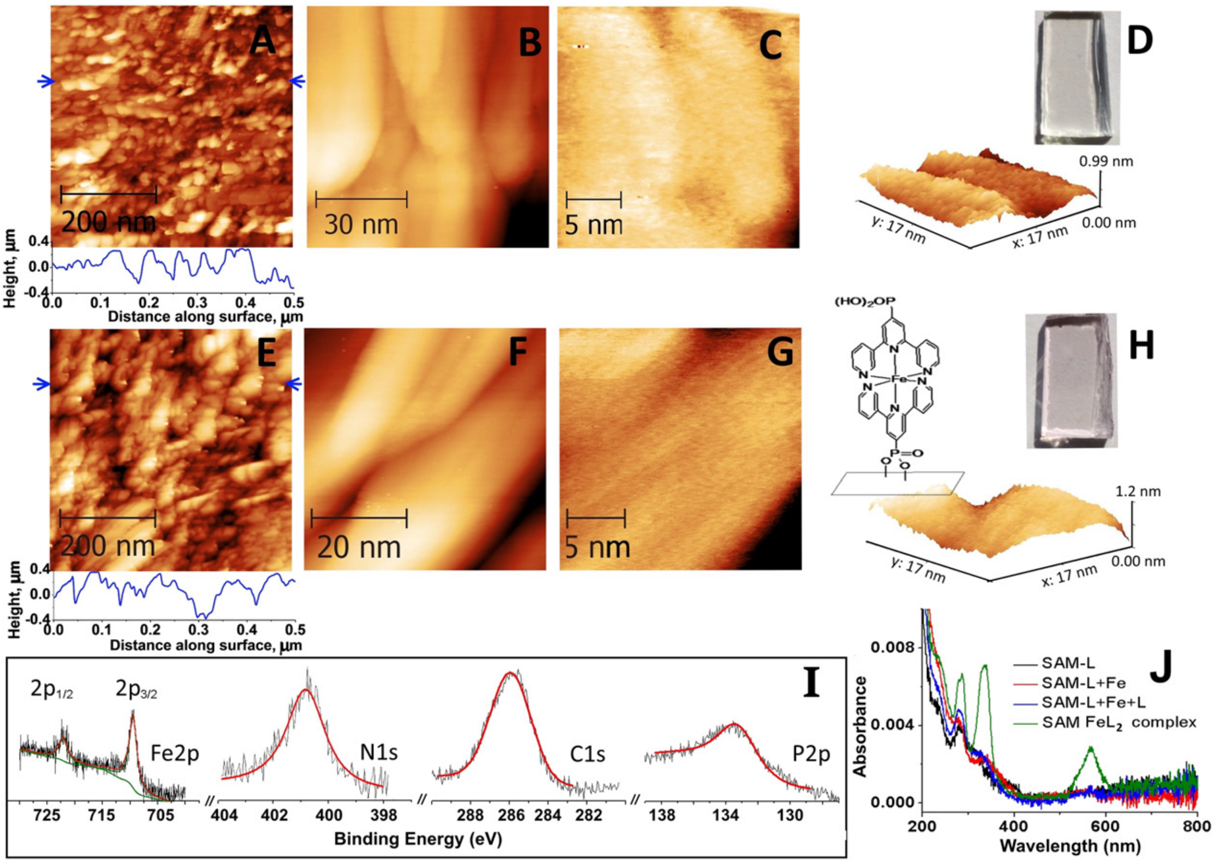

Fig. 1. Representative STM images: (A–D) bare FTO/glass and (E–H) SAM-Fe$\mathbf{L}_2$ on FTO/glass slides. Representative XPS data for SAM-Fe$\mathbf{L}_2$ on FTO/glass slides (I): Fe (2p), N (1 s), C (1 s), and P (2p). The black line shows the experimental data, while the coloured lines are the overall fitted spectra. UV–vis spectra (J) of as-deposited SAM-**L** (black), followed by its step by step treatment with Fe^{2+} aqueous solution (red) and solution of **L** (blue) show no significant change of the spectra suggesting no Fe$\mathbf{L}_2$ complex formation. In comparison, UV–vis spectrum of Fe$\mathbf{L}_2$ complex pre-formed in solution and then deposited as a SAM on quartz surface (green) shows a distinguishable characteristic peak at 569 nm.

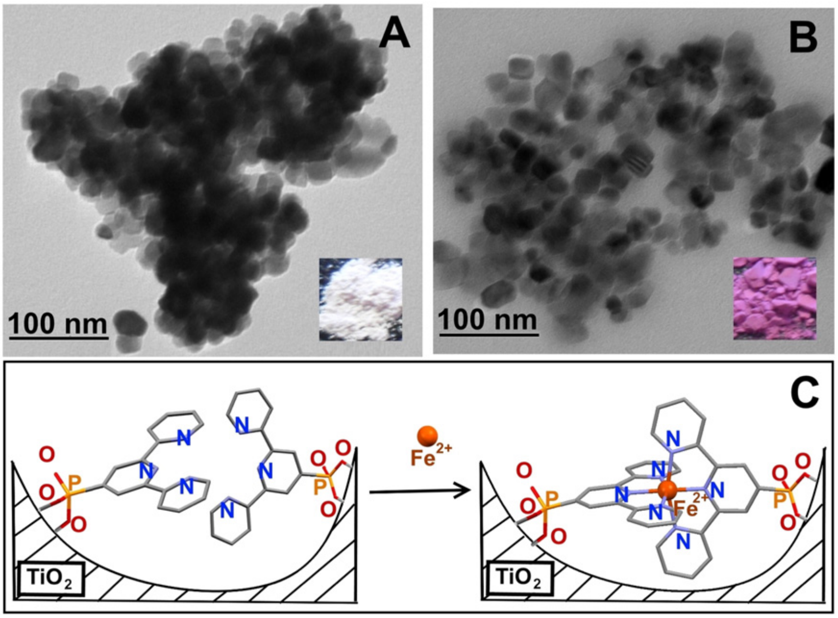

Fig. 2. Representative TEM images of commercial TiO_2, anatase nanopowder, functionalized by **L**. **A**: before and **B**: after treatment with aqueous Fe^{2+} solutions. **C**: Proposed reaction mechanism of Fe^{2+} interactions with **L** molecules bound to TiO_2 nanopowder surface.

surfaces with molecular densities close to those found in single crystals [55]. Taking this into account, we prepared the complex Fe**L**$_2$ and deposited it onto FTO/glass and quartz surfaces (Fig. 1). Scanning tunneling microscopy (STM) analysis shows that the roughness of the Fe**L**$_2$ functionalized FTO/glass surface (Fig. 1E–H) is very similar to that of unfunctionalized FTO/glass (Fig. 1 A–D), which suggest the formation of a monolayer. The embedding of the complex on the quartz or FTO/glass surfaces can be easily observed by the naked eye. On the contrary, anchoring of **L** on quartz surfaces does not result in any visible colour. However, this process could be monitored by UV–vis spectroscopy which confirms the formation of a monolayer of **L** on the surface (Fig. 1J). Moreover, insertion of quartz slides with the pre-deposited **L** in 0.1 mM solution of Fe^{2+} results in insignificant changes in UV–vis spectra of the quartz substrates. Further immersion of these slides into a 0.1 mM solution of the ligand does not change the UV–vis spectra of surface bonded layer at 560 nm, which is characteristic of a metal to ligand charge transfer (MLCT) transition for a Fe**L**$_2$ type complex [56], suggesting that Fe^{2+} did not incorporate into the ligand anchored to the surface. In contrast, preparation of the Fe**L**$_2$ complex in solution followed by its deposition on quartz slides results in a significant increase of intensities at 287 nm and 332 nm as well as the appearance of a new peak at 569 nm (Fig. 1J). The red shift of the on-surface Fe**L**$_2$ monolayer with respect to Fe**L**$_2$ in aqueous solution (278, 321 and 560 nm, respectively) is the consequence of the change in the microenvironment of Fe**L**$_2$ in these two different media [57].

Further characterization of the Fe**L**$_2$ complex deposited on glass surface by XPS (Fig. 1I) verifies the presence of iron, nitrogen, carbon and phosphorous on the surface within ratios close to the molecular stoichiometry. The binding energy of any XPS peak depends on the oxidation state of an element and on its binding site on the surface. Thus, the

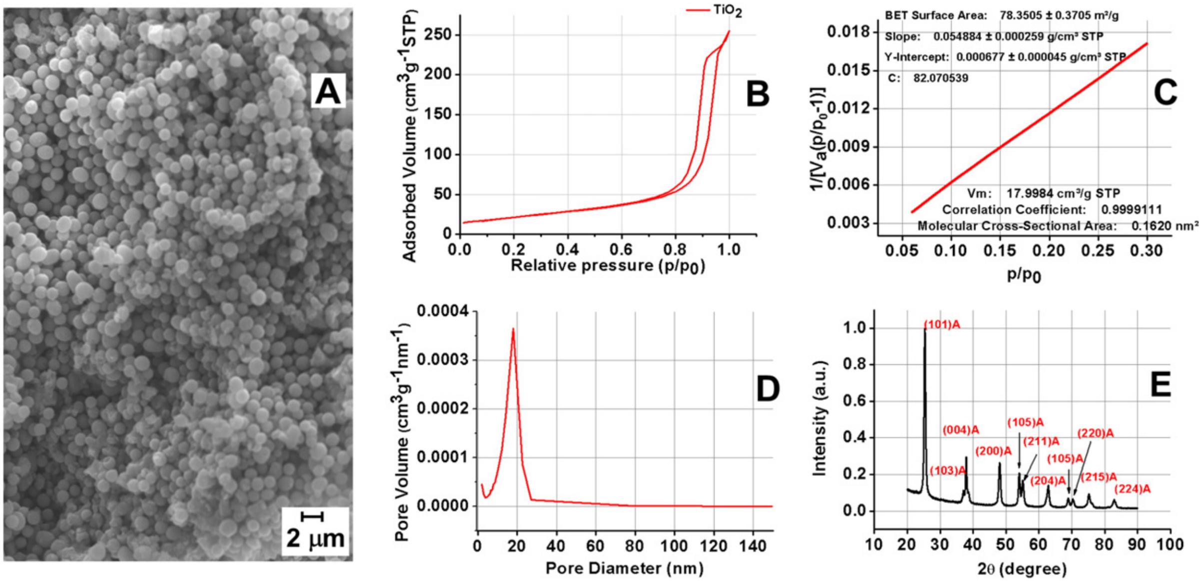

Fig. 3. A: Typical SEM image of synthesized mesoporous TiO_2 NPs. B: Adsorption-desorption isotherm for mesoporous TiO_2 NPs. C: BET linear region fit for TiO_2 mesoporous beads. D: Pore diameter distribution obtained by BJH method. E: Powder diffraction spectrum of mesoporous TiO_2 beads.

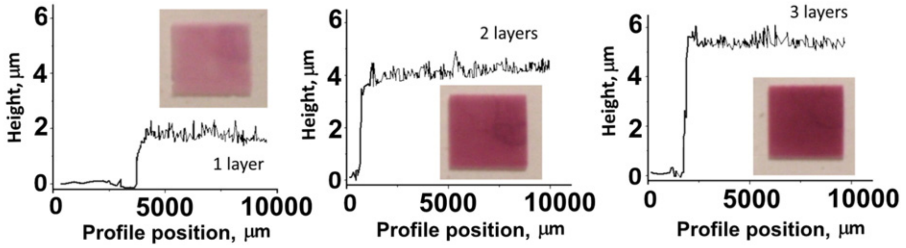

Fig. 4. Typical profilometry curves of the mesoporous TiO_2 nanopowder deposited and sintered on FTO/glass substrates show thickness of each layer of 2 µm. Inserts: images of corresponding films after application of 150 µL of 45 ppm aqueous Fe^{2+} solution.

binding energy of the Fe $2p_{3/2}$ peak is located at 709.6 eV; and that of Fe $2p_{1/2}$ can be seen at 722.1 eV. Both peaks are characteristic for Fe^{2+}. The N 1 s peak at 400.9 eV is evidently associated with aromatic nitrogen, which provides the electron density to form the complex. The C 1 s peak is centered at 286.0 eV, which is in good agreement with aromatic carbon. An asymmetric broad peak observed at 133.6 eV is due to the overlapping of the P $2p_{3/2}$ and P $2p_{1/2}$ components, which is characteristic for phosphates.

To estimate the packing density of Fe**L**$_2$ molecules on quartz surfaces, the two-dimensional surface concentration, $\Gamma_{\text{monolayer}}$ (molecules·cm^{-2}), was calculated based on UV–vis data [40]. For this Fe**L**$_2$ solution molar extinction coefficient of $\varepsilon_{560\ \text{nm}} = 11970\ M^{-1}\ cm^{-1}$ and the absorbance observed for the monolayer (see Fig. 1J and Experimental section) resulted in a $\Gamma_{\text{monolayer}}$ of $7\cdot10^{-13}$ molecules·cm^{-2}. This corresponds to a surface area occupied by one molecule of Fe**L**$_2$ equal to 1.43 nm^2. The surface area estimated from the crystal structure of Fe**L**$_2$ is close to 1.2 nm^2 per molecule. The surface concentration of **L** was found to be 1.23 molecules·nm^{-2} that corresponds to 0.81 nm^2 per molecule of **L**. This suggests that **L** forms well-ordered and densely packed monolayers on relatively smooth surfaces and thus due to the intermolecular π-π interactions the rotation of the terpy moieties that are anchored to the surface is limited. Reduced flexibility of the terpy moieties on the surface, in turn, restricts the participation of two neighboring surface anchored ligands in complex formation.

We propose that when a high specific surface area substrate is functionalized with **L**, a certain fraction of these molecules might be available for Fe**L**$_2$ complex formation. Indeed, modification of commercially available titanium (IV) oxide anatase nanopowder by **L** followed by treatment of the functionalized **L**-TiO_2 NPs with Fe^{2+} solutions results in significant colour change (Fig. 2A & B insets). Particle size distribution of the nanopowder functionalized by **L** before (Fig. 2A) and after treatment with Fe^{2+} (Fig. 2B) remains very similar to 25 nm in diameter as declared for bare TiO_2 nanopowder by the manufacturer.

To make this system more practical and applicable for easy and rapid Fe^{2+} detection, a paste comprised of high (70–110 $m^2\ g^{-1}$) specific surface area Evonik P90 commercial TiO_2 nanopowder (scaffold material), ethyl cellulose (binder and thickening agent) and α-terpineol (solvent) has been prepared according to a previously reported procedure [44]. The paste was screen-printed onto 1 × 1 cm squares of soda lime glass, which had been pretreated with basic piranha solution, dried, and thermally treated in air. One, three, and six layers (2 µm each) were screen-printed one by one to increase the volume of the detecting cell thus tuning the detection range. When prepared, layered screen-printed P90 TiO_2 films were functionalized via immersion into a 0.65 mM aqueous solution of **L** for 1 h followed by washing with isopropyl alcohol (3 × 3 mL) and dried by a stream of air. The resulting sensing strips were treated with 150 µL of 45 ppm aqueous Fe^{2+} solution. All sensing strips turned deep magenta with comparable intensity. These results confirm that the novel material can detect Fe^{2+} in an aqueous solution. However, we believe that small particles size (typically 15 nm) of P90 favors sintering processes resulting in the formation of surfaces where diffusion through the layers is impeded. As such only a reduced amount of surface remains accessible for the functionalization by the molecular receptor **L**, which is active in metal-ion recognition. As a result, P90 TiO_2 based screen-printed materials do not allow reasonable control of sensitivity since no significant difference in colour intensity was observed between one and multiple (up to 6 layers) screen-printed films.

To validate our initial assumption regarding the role of nanoparticle dimensions and pore size, we synthesized TiO_2 nanoparticles (crystallites size estimated by XRD to be ~25 nm) arranged in large (1263 ± 86 nm in diameter) mesoporous hierarchical spheres (beads), Fig. 3A. The presence of mesopores (IUPAC classification: 2–50 nm) is easily recognizable by the characteristic hysteresis in the N_2 adsorption-desorption graph (Fig. 3B). Specific surface area determined by the BET (Brunauer-Emmett-Teller) method has been found to be 78.4 ± 0.4 $m^2\ g^{-1}$. Pore size distribution was determined by the BJH (Barret-Joyner-Halenda) method (Fig. 3D) and it has revealed a pore diameter distribution peaking at ca. 18 nm. Thus, although specific surface area of synthesized mesoporous TiO_2 nanoparticles is comparable to that of P90 one, the former are characterized by an almost monodisperse porosity stemming from spherical organization of randomly oriented nanocrystals. Moreover, the spherical shape of mesoporous TiO_2 beads minimize the surface energy tend to avoid surface shrinkage during the annealing process. Further analysis of the synthesized mesoporous TiO_2 material by X-ray powder diffraction followed by Rietveld refinement analysis (MAUD software) [45] results in the following lattice parameters: a = 3.782 ± 0.001 Å, c = 9.492 ± 0.003 Å. The data are in good agreement with the reference data (a = 3.784479 Å, c = 9.5137 Å) for the tetragonal crystal structure of anatase (space group *i*41/*amd*).

Synthesis of mesoporous beads followed by their layer by layer additive screen-printing and functionalization by **L**, results in Fe^{2+} detecting films with a well tunable thickness (Fig. 4). These mesoporous screen-printed materials, in contrast to ones made from commercially available P90 TiO_2 NPs, benefit from better water diffusion and could be applied for quantitative Fe^{2+} detection. Dropwise addition of 150 µL of a

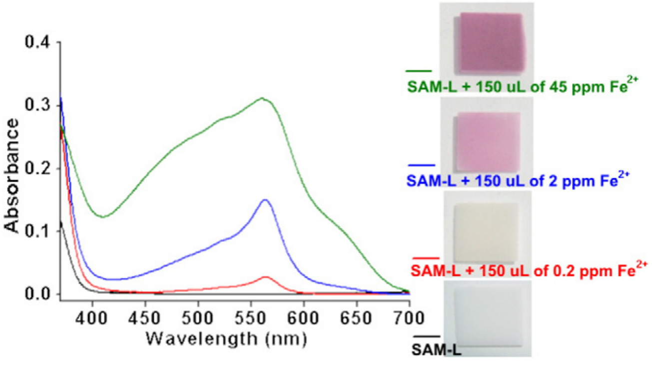

Fig. 5. Diffuse reflectance UV–vis spectra and optical photographs of mesoporous TiO_2 screen-printed films (3 screen-printed layers) functionalized by **L** before and after treatment with 150 µL of aqueous Fe^{2+} solutions. The characteristic peak at 560 nm confirms the formation of the Fe**L**$_2$ complex.

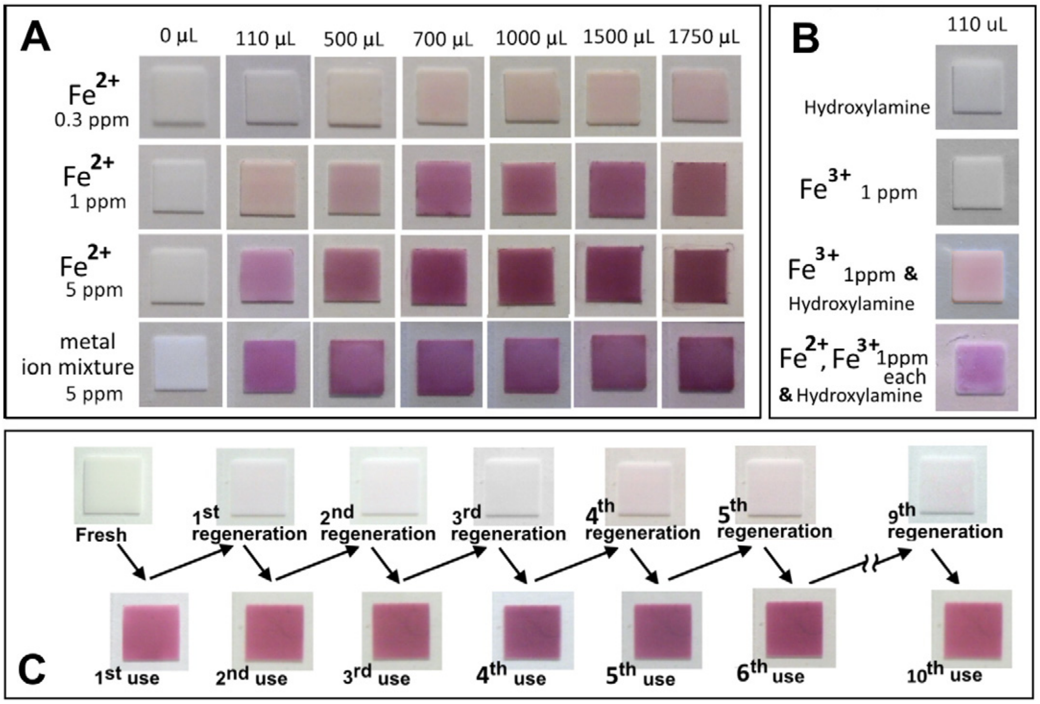

Fig. 6. A: Colour wheel showing the colour change of detecting film after applying varying volumes of aqueous Fe^{2+} solutions: 0.3 ppm (upper row), 1 ppm (2nd line from the top), 5 ppm (3rd line), and a mixture of metal ions (including Fe^{2+}), 5 ppm each (bottom row) see main text for details. B: Aqueous solutions of hydroxylamine do not change the colour of the detecting film. Using this reagent to reduce Fe^{3+} to Fe^{2+} makes it possible to detect the total amount of iron in solution. C: Detecting films can be recovered by EDTA and reused, see main text for details.

45 ppm aqueous solution of Fe^{2+} on 1, 2, and 3 layered screen-printed films of mesoporous TiO_2 nanopowder results in a rapid colour change from white to 3 shades of purple. The colour intensity increases as the number of screen-printed layers increase (Fig. 4). This observation suggests that both mesoporosity and particle size are important factors allowing for modulation of sensitivity and better quantitative analysis.

Three layered (6 µm height) screen-printed films of mesoporous TiO_2 functionalized by **L** (further – detecting films) were further studied to determine the detectable Fe^{2+} concentration range. Applying 150 µL of 0.2 ppm, 2 ppm, and 45 ppm solutions of Fe^{2+} to the detecting films results in the appearance of a peak at 560 nm on the diffuse reflectance UV–vis spectra (Fig. 5). A slight colour change takes place in the case of 0.2 ppm Fe^{2+} solution; but the colour change observed when 2 ppm and 45 ppm solutions were used could be easily distinguished by the naked eye.

According to the U.S. Environmental Protection Agency secondary drinking water standard and Guidelines for Canadian drinking water quality, maximum contaminant level of iron is 0.3 ppm. The United Nations Food and Agriculture Organization recommends a level of 5 ppm for irrigation waters. On the other hand, iron in groundwater (in ferrous i.e. Fe^{2+} form) varies from 0.1 to 10 ppm [58]. Needless to say, the development of inexpensive, reusable and reliable materials which are able to rapidly detect iron in field conditions is in high demand. To insure our detecting films can be used as a material for Fe^{2+} determination, certain amounts of aqueous Fe^{2+} solutions were added to each film creating an appropriate colour wheel (Fig. 6).

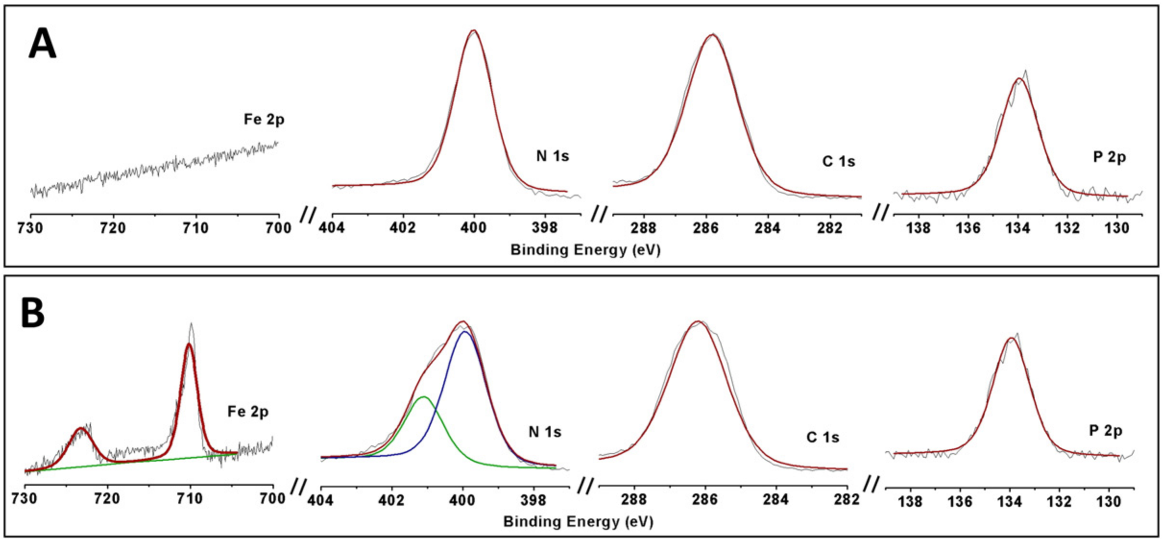

Fig. 7. Comparative X-ray photoelectron spectra of **L** anchored to mesoporous TiO_2 screen-printed films A: before and B: after application of 110 µL of 5 ppm aqueous Fe^{2+} solution.

The resulting colour wheel is consistent with our expectations: the colour intensity depends on the amount of Fe^{2+} added. This permits the visual quantification of iron cations in aqueous solutions ranging from 0.3 ppm to 5 ppm. To investigate the detecting films' selectivity towards Fe^{2+} in the presence of potentially interfering ions, an aqueous solution containing Na^{+}, Fe^{2+}, Cr^{3+}, Sn^{2+}, Ca^{2+}, Li^{+}, Co^{2+}, Mg^{2+}, Cu^{2+}, Cs^{+}, Ni^{2+}, Ba^{2+}, K^{+}, and Mn^{2+} (5 ppm each) was prepared and portionwise applied to the detecting films. Fig. 6A clearly shows that the detecting films treated with the multiple ion solution have a similar colour intensity to those treated with solution containing solely Fe^{2+}. This shows the material is highly selective for Fe^{2+} determination.

In addition, we studied the ability of our screen-printed material to detect Fe^{3+} ions in the aqueous solutions. Aqueous solutions of Fe^{3+} do not result in a change of colour of the detecting film. However, aqueous Fe^{3+} can be detected if reduced by hydroxylamine to Fe^{2+} [59] (Fig. 6B).

Notably, the detecting films can be reused after immersion into a 0.5 mM solution of ethylenediaminetetraacetic acid disodium salt (EDTA) for 48 h. Iron release from the films into the EDTA solution can be monitored by the visual colour change of the films. Fig. 6C shows the behavior of the colour on the films for 10 successive cycles of resetting. No evidence of degradation of sensitivity can be detected. Increasing the temperature of the EDTA solution to 80 °C reduces the film recovery time to 24 h.

XPS analysis of detecting films before interaction with Fe^{2+} confirms the presence of N, C, and P of **L** on the surface (Fig. 7A). The sharp (with full width at half-maximum (FWHM) of 1.9 eV) N 1 s peak is centered at 400.0 eV. The C 1 s peak is centered at 285.8 eV, as expected for aromatic carbon. An asymmetric broad peak observed at 133.8 eV is characteristic for P 2p. The N:C:P ratio of 2.5:17.4:1.0 is close to 3:15:1 of **L** molecular stoichiometry. When 110 μL of 5 ppm aqueous Fe^{2+} solution was applied to the detecting film (Fig. 7B) the appearance of two new peaks was observed. The peaks with the binding energies of 709.9 eV and 722.4 eV are characteristic for Fe 2p$_{3/2}$ and Fe 2p$_{1/2}$ of Fe^{2+}, respectively. Interestingly, the P 2p peak position remains unchanged within the experimental error (133.8 eV) after Fe^{2+} solution application. The C 1 s peak is insignificantly shifted to 286.1 eV. The N 1 s peak undergoes a significant change and now can be deconvoluted using a Powell peak-fitting algorithm with FWHM of 1.3 eV yielding a peak centered at 400.0 eV and a new peak centered at 401.1 eV. This value is close to 400.9 eV, which was observed for the Fe**L**$_2$ complex deposited on the FTO surface (Fig. 1I). The P:Fe ratio is 1:0.01 suggesting that as expected, only a fraction of **L** molecules are able to form the Fe**L**$_2$ complex. However, assuming that the complex formation takes place not on the flat surface, but inside the pores, the iron content can be underestimated due to the signal attenuation.

4. Conclusions

We observed that 2,2′:6′,2″-terpyridin-4′-ylphosphonic acid, **L**, forms dense SAMs on FTO/glass and quartz surfaces. Due to the close packing of the **L** molecules, these SAMs, once formed, cannot react with Fe^{2+} to form the Fe**L**$_2$ complex. On the other hand, in solution, the pre-formed Fe**L**$_2$ complex forms dense SAMs on the glass surface which are observable by the naked eye as pink colouring of the glass. Deposition of **L** as SAMs on high surface area TiO$_2$ nanostructures results in a situation where some of the **L**s are able to form Fe**L**$_2$ complex. The formation of the Fe^{2+} complex, in turn, leads to significant colouring of the material. To improve detection abilities and adjust the Fe^{2+} detection limits, large mesoporous TiO$_2$ beads were synthesized and screen-printed on glass or FTO/glass slides. Functionalization of these beads by **L** results in reusable detecting films that are able to quantify Fe^{2+} in aqueous solutions with a concentration range of 0.3 to 5 ppm. The selectivity of Fe^{2+} detection in the presence of 13 other metal ions was shown. This material is expected to be useful for the design of more advanced efficient optical, chemical, and biological sensors. Such sensors would benefit from high accuracy, reliability, portability, and cost effectiveness.

Acknowledgment

Research supported by the University of Ontario Institute of Technology start-up grant (156057-2700) and NSERC Discovery grant (RGPIN-2016-05823).

References

[1] N. Kaur, S. Kumar, Colorimetric metal ion sensors, Tetrahedron 67 (48) (2011) 9233–9264.

[2] G. Korotcenkov, B.K. Cho, Instability of metal oxide-based conductometric gas sensors and approaches to stability improvement (short survey), Sensors Actuators B 156 (2) (2011) 527–538.

[3] W.E. Duckworth, Sensor materials, Mater. Des. 9 (2) (1988) 72–77.

[4] E.C. Constable, The Coordination Chemistry of 2,2′:6′,2″-Terpyridine -Terpyridine and Higher Oligopyridines, vol. 30Academic Press, 1986 69–121.

[5] J.M. Hamilton, M.J. Anhorn, K.A. Oscarson, J.H. Reibenspies, R.D. Hancock, Complexation of metal ions, including alkali-earth and lanthanide(III) ions, in aqueous solution by the ligand 2,2′,6′,2″-terpyridyl, Inorg. Chem. 50 (7) (2011) 2764–2770.

[6] F. Barigelletti, L. Flamigni, G. Calogero, L. Hammarstrom, J.-P. Sauvage, J.-P. Collin, A functionalized ruthenium(II)-bis-terpyridine complex as a rod-like luminescent sensor of zinc(II), Chem. Commun. (21) (1998) 2333–2334.

[7] R.D. Hancock, The pyridyl group in ligand design for selective metal ion complexation and sensing, Chem. Soc. Rev. 42 (4) (2013) 1500–1524.

[8] C. Bhaumik, S. Das, D. Saha, S. Dutta, S. Baitalik, Synthesis, characterization, photophysical, and anion-binding studies of luminescent heteroleptic bis-tridentate ruthenium(II) complexes based on 2,6-bis(benzimidazole-2-yl)pyridine and 4′-substituted 2,2′:6′,2″ terpyridine derivatives, Inorg. Chem. 49 (11) (2010) 5049–5062.

[9] G. Baggi, M. Boiocchi, C. Ciarrocchi, L. Fabbrizzi, Enhancing the anion afinity of urea-based receptors with a Ru(terpy)$_2^{2+}$ chromophore, Inorg. Chem. 52 (9) (2013) 5273–5283.

[10] A.R. Rabindranath, A. Maier, M. Schäfer, B. Tieke, Luminescent and ionochromic polyiminofluorene with conjugated terpyridine substituent groups, Macromol. Chem. Phys. 210 (8) (2009) 659–668.

[11] Y. Hong, S. Chen, C.W.T. Leung, J.W.Y. Lam, J. Liu, N.-W. Tseng, R.T.K. Kwok, Y. Yu, Z. Wang, B.Z. Tang, Fluorogenic Zn(II) and chromogenic Fe(II) sensors based on terpyridine-substituted tetraphenylethenes with aggregation-induced emission characteristics, ACS Appl. Mater. Interfaces 3 (9) (2011) 3411–3418.

[12] P. Wang, T.-a. Okamura, H.-P. Zhou, W.-Y. Sun, Y.-P. Tian, Metal complex with terpyridine derivative ligand as highly selective colorimetric sensor for iron(III), Chin. Chem. Lett. 24 (1) (2013) 20–22.

[13] S.M. Brombosz, A.J. Zucchero, R.L. Phillips, D. Vazquez, A. Wilson, U.H.F. Bunz, Terpyridine-based cruciform − Zn^{2+} complexes as anion-responsive fluorophores, Org. Lett. 9 (22) (2007) 4519–4522.

[14] X. Peng, Y. Xu, S. Sun, Y. Wu, J. Fan, A ratiometric fluorescent sensor for phosphates: Zn^{2+}-enhanced ICT and ligand competition, Org. Biomol. Chem. 5 (2) (2007) 226–228.

[15] M. Ali, S. Nasir, Q.H. Nguyen, J.K. Sahoo, M.N. Tahir, W. Tremel, W. Ensinger, Metal ion affinity-based biomolecular recognition and conjugation inside synthetic polymer nanopores modified with iron–terpyridine complexes, J. Am. Chem. Soc. 133 (43) (2011) 17307–17314.

[16] T.A. Ali, G.G. Mohamed, A.H. Farag, Electroanalytical studies on Fe(III) ion-selective sensors based on 2-methyl-6-(4-methylenecyclohex-2-en-1-yl)hept-2-en-4-one ionophore, Int. J. Electrochem. Sci. 10 (1) (2015) 564–578.

[17] Q. Zhang, X. Tian, Z. Hu, C. Brommesson, J. Wu, H. Zhou, S. Li, J. Yang, Z. Sun, Y. Tian, K. Uvdal, A series of Zn(II) terpyridine complexes with enhanced two-photon-excited fluorescence for in vitro and in vivo bioimaging, J. Mater. Chem. B 3 (36) (2015) 7213–7221.

[18] A. Wild, A. Winter, F. Schlutter, U.S. Schubert, Advances in the field of pi-conjugated 2,2′:6′,2″-terpyridines, Chem. Soc. Rev. 40 (3) (2011) 1459–1511.

[19] M. Trigo-López, A. Muñoz, S. Ibeas, F. Serna, F.C. García, J.M. García, Colorimetric detection and determination of Fe(III), Co(II), Cu(II) and Sn(II) in aqueous media by acrylic polymers with pendant terpyridine motifs, Sensors Actuators B 226 (2016) 118–126.

[20] Q. Ru, Z. Xue, Y. Wang, Y. Liu, H. Li, Luminescent materials of europium(III) coordinated by a terpyridine-functionalized poly(ionic liquid), Eur. J. Inorg. Chem. 2014 (3) (2014) 469–474.

[21] D. Wang, H. Wang, H. Li, Novel luminescent soft materials of terpyridine-containing ionic liquids and europium(III), ACS Appl. Mater. Interfaces 5 (13) (2013) 6268–6275.

[22] M. Ichikawa, T. Yamamoto, H.-G. Jeon, K. Kase, S. Hayashi, M. Nagaoka, N. Yokoyama, Benzene substituted with bipyridine and terpyridine as electron-transporting materials for organic light-emitting devices, J. Mater. Chem. 22 (14) (2012) 6765.

[23] A.E. Taouil, J. Husson, L. Guyard, Synthesis and characterization of electrochromic [Ru(terpy)$_2$ selenophene]-based polymer film, J. Electroanal. Chem. 728 (2014) 81–85.

[24] A. Winter, U.S. Schubert, New polyester-based terpyridine macroligands and their blue Iron(II) complexes, Macromol. Chem. Phys. 208 (18) (2007) 1956–1964.

[25] C. Monnereau, J. Gomez, E. Blart, F. Odobel, S. Wallin, A. Fallberg, L. Hammarström, Photoinduced electron transfer in platinum(II) terpyridinyl acetylide complexes connected to a porphyrin unit, Inorg. Chem. 44 (13) (2005) 4806–4817.

[26] F. Camerel, R. Ziessel, B. Donnio, D. Guillon, Engineering of an iron–terpyridine complex with supramolecular gels and mesomorphic properties, New J. Chem. 30 (2) (2006) 135–139.

[27] H.A. Saadeh, E.A.A. Shairah, N. Charef, M.S. Mubarak, Synthesis and adsorption properties, toward some heavy metal ions, of a new polystyrene-based terpyridine polymer, J. Appl. Polym. Sci. 124 (4) (2012) 2717–2724.

[28] S. Köytepe, M.H. Demirel, A. Gültek, T. Seçkin, Metallo-supramolecular materials based on terpyridine-functionalized polyhedral silsesquioxane, Polym. Int. 63 (4) (2014) 778–787.

[29] A.O.T. Patrocinio, K.P.M. Frin, N.Y. Murakami Iha, Solid state molecular device based on a rhenium(I) polypyridyl complex immobilized on TiO_2 films, Inorg. Chem. 52 (10) (2013) 5889–5896.

[30] R. Sakamoto, S. Katagiri, H. Maeda, H. Nishihara, Bis(terpyridine) metal complex wires: excellent long-range electron transfer ability and controllable intrawire redox conduction on silicon electrode, Coord. Chem. Rev. 257 (9–10) (2013) 1493–1506.

[31] R. Sakamoto, Y. Ohirabaru, R. Matsuoka, H. Maeda, S. Katagiri, H. Nishihara, Orthogonal bis(terpyridine)-Fe(II) metal complex oligomer wires on a tripodal scaffold: rapid electron transport, Chem. Commun. 49 (64) (2013) 7108–7110.

[32] A. Winter, C. Friebe, M.D. Hager, U.S. Schubert, Advancing the solid state properties of metallo-supramolecular materials: poly(ε-caprolactone) modified π-conjugated bis(terpyridine)s and their Zn(II) based metallo-polymers, Macromol. Rapid Commun. 29 (20) (2008) 1679–1686.

[33] D. Zhou, Q.-Y. Cheng, Y. Cui, T. Wang, X. Li, B.-H. Han, Graphene–terpyridine complex hybrid porous material for carbon dioxide adsorption, Carbon 66 (2014) 592–598.

[34] G.T. Morgan, F.H. Burstall, 3. Dehydrogenation of pyridine by anhydrous ferric chloride, J. Chem. Soc. (1932) 20–30.

[35] K. Takada, R. Sakamoto, S.-T. Yi, S. Katagiri, T. Kambe, H. Nishihara, Electrochromic bis(terpyridine)metal complex nanosheets, J. Am. Chem. Soc. 137 (14) (2015) 4681–4689.

[36] E.C. Constable, Modern Terpyridine Chemistry. By Ulrich S. Schubert, Harald Hofmeier and George R. Newkome, Angew. Chem. Int. Ed. 46 (16) (2007) 2748–2749.

[37] E.C. Constable, M.D. Ward, Synthesis and co-ordination behaviour of 6′,6″-bis(2-pyridyl)-2,2′: 4,4″: 2″,2′“-quaterpyridine; ‘back-to-back’ 2,2′: 6′,2”-terpyridine, J. Chem. Soc. Dalton Trans. (4) (1990) 1405–1409.

[38] P. Péchy, F.P. Rotzinger, M.K. Nazeeruddin, O. Kohle, S.M. Zakeeruddin, R. Humphry-Baker, M. Grätzel, Preparation of phosphonated polypyridyl ligands to anchor transition-metal complexes on oxide surfaces: application for the conversion of light to electricity with nanocrystalline TiO2 films, J. Chem. Soc. Chem. Commun. (1) (1995) 65–66.

[39] K.T. Potts, D. Konwar, Synthesis of 4′-vinyl-2,2′:6′,2″-terpyridine, J. Organomet. Chem. 56 (15) (1991) 4815–4816.

[40] X. Guo, M. Myers, S. Xiao, M. Lefenfeld, R. Steiner, G.S. Tulevski, J. Tang, J. Baumert, F. Leibfarth, J.T. Yardley, M.L. Steigerwald, P. Kim, C. Nuckolls, Chemoresponsive monolayer transistors, Proc. Natl. Acad. Sci. U. S. A. 103 (31) (2006) 11452–11456.

[41] N.O. Laschuk, I.I. Ebralidze, D. Spasyuk, O.V. Zenkina, Multi-readout logic gate for selective metal ions detection in parts per billion levelsSubmitted 2016.

[42] D. Chen, L. Cao, F. Huang, P. Imperia, Y.-B. Cheng, R.A. Caruso, Synthesis of monodisperse mesoporous titania beads with controllable diameter, high surface areas, and variable pore diameters (14–23 nm), J. Am. Chem. Soc. 132 (12) (2010) 4438–4444.

[43] A. Latini, C. Cavallo, F.K. Aldibaja, D. Gozzi, D. Carta, A. Corrias, L. Lazzarini, G. Salviati, Efficiency improvement of DSSC photoanode by scandium doping of mesoporous titania beads, J. Phys. Chem. C 117 (48) (2013) 25276–25289.

[44] S. Ito, P. Chen, P. Comte, M.K. Nazeeruddin, P. Liska, P. Péchy, M. Grätzel, Fabrication of screen-printing pastes from TiO_2 powders for dye-sensitised solar cells, Prog. Photovolt. Res. Appl. 15 (7) (2007) 603–612.

[45] L. Lutterotti, Total pattern fitting for the combined size–strain–stress–texture determination in thin film diffraction, Nucl. Inst. Methods Phys. Res. B 268 (3–4) (2010) 334–340.

[46] C.D. Wagner, Sensitivity factors for XPS analysis of surface atoms, J. Electron Spectrosc. Relat. Phenom. 32 (2) (1983) 99–102.

[47] G. Guerrero, J.G. Alauzun, M. Granier, D. Laurencin, P.H. Mutin, Phosphonate coupling molecules for the control of surface/interface properties and the synthesis of nanomaterials, Dalton Trans. 42 (35) (2013) 12569–12585.

[48] M. Becuwe, P. Rouge, C. Gervais, M. Courty, A. Dassonville-Klimpt, P. Sonnet, E. Baudrin, A new sensitive organic/inorganic hybrid material based on titanium oxide for the potentiometric detection of iron(III), J. Colloid Interface Sci. 388 (1) (2012) 130–136.

[49] G.J. Ruiterkamp, M.A. Hempenius, H. Wormeester, G.J. Vancso, Surface functionalization of titanium dioxide nanoparticles with alkanephosphonic acids for transparent nanocomposites, J. Nanopart. Res. 13 (7) (2010) 2779–2790.

[50] P. Thissen, M. Valtiner, G. Grundmeier, Stability of phosphonic acid self-assembled monolayers on amorphous and single-crystalline aluminum oxide surfaces in aqueous solution, Langmuir 26 (1) (2010) 156–164.

[51] C. Tudisco, V. Oliveri, M. Cantarella, G. Vecchio, G.G. Condorelli, Cyclodextrin anchoring on magnetic Fe3O4 nanoparticles modified with phosphonic linkers, Eur. J. Inorg. Chem. 2012 (32) (2012) 5323–5331.

[52] H. Ma, O. Acton, D.O. Hutchins, N. Cernetic, A.K.Y. Jen, Multifunctional phosphonic acid self-assembled monolayers on metal oxides as dielectrics, interface modification layers and semiconductors for low-voltage high-performance organic field-effect transistors, Phys. Chem. Chem. Phys. 14 (41) (2012) 14110–14126.

[53] P.J. Hotchkiss, S.C. Jones, S.A. Paniagua, A. Sharma, B. Kippelen, N.R. Armstrong, S.R. Marder, The modification of indium tin oxide with phosphonic acids: mechanism of binding, tuning of surface properties, and potential for use in organic electronic applications, Acc. Chem. Res. 45 (3) (2012) 337–346.

[54] A. Vega, P. Thissen, Y.J. Chabal, Environment-controlled tethering by aggregation and growth of phosphonic acid monolayers on silicon oxide, Langmuir 28 (21) (2012) 8046–8051.

[55] M. McDowell, I.G. Hill, J.E. McDermott, S.L. Bernasek, J. Schwartz, Improved organic thin-film transistor performance using novel self-assembled monolayers, Appl. Phys. Lett. 88 (7) (2006) 073505.

[56] J.K. Klosterman, A. Linden, D.K. Frantz, J.S. Siegel, Manisyl-substituted polypyridine coordination compounds: metallo-supramolecular networks of interdigitated double helices assembled via CH-π and π-π interactions, Dalton Trans. 39 (6) (2010) 1519–1531.

[57] F. Guérin, Y. Tian, J.H. Fendler, Dihexadecyl phosphate monolayer supported $[Ru(bpy)]_3^{2+}$ crystallites investigated by near-field scanning optical microscopy, J. Phys. Chem. B 103 (37) (1999) 7882–7888.

[58] Standard Methods for the Examination of Water and Wastewater, 21 ed. The American Public Health Association, The American Water Works Association and The Water Environment Federation, 2005, http://www.standardmethods.org.

[59] R.L. Morris, Determination of iron in water in the presence of heavy metals, Anal. Chem. 24 (1952) 1376–1378.